

Hybrid model calculations of direct photons in high-energy nuclear collisions

Björn Bäuchle^{1, 2, *} and Marcus Bleicher²

¹*Frankfurt Institute for Advanced Studies, Frankfurt am Main, Germany*

²*Institut für Theoretische Physik, Goethe-Universität, Frankfurt am Main, Germany*

Direct photon emission in heavy-ion collisions is calculated within a relativistic micro+macro hybrid model and compared to the microscopic transport model UrQMD. In the hybrid approach, the high-density part of the evolution is replaced by an ideal 3-dimensional hydrodynamic calculation. This allows to examine the effects of viscosity and full local thermalization, in comparison of the transport model to the ideal fluid-dynamics. We study the origin of high- p_{\perp} photons as well as the impact of elementary high- \sqrt{s} collisions. We further explore the contribution of different production channels and non-thermal radiation to the spectrum of direct photons. Detailed comparison to the measurements by the WA98-collaboration are also undertaken.

I. INTRODUCTION

Creating and studying high-density and -temperature nuclear matter is the major goal of heavy-ion experiments. A state of quasi-free partonic degrees of freedom, the Quark-Gluon-Plasma (QGP) [1, 2] may be formed, if the energy density in the reaction is high enough. Strong jet quenching, high elliptic flow and other observations made at the Relativistic Heavy Ion Collider (BNL-RHIC) suggest the successful creation of a strongly coupled QGP (sQGP) at these energies [3–6]. Possible evidence for the creation of this new state of matter has also been put forward by collaborations at the Super Proton Synchrotron (CERN-SPS), as for instance the step in the mean transverse mass excitation function of protons, kaons and pions and the enhanced K^+/π^+ -ratio [7].

Out of the many possible observables, electromagnetic probes have the advantage of leaving the hot and dense region undisturbed: once they are created, they escape freely from the reaction zone, due to their negligible rescattering cross-sections. Besides dileptons, direct photon emission is therefore of greatest interest to gain insight into the early, hot and therefore possibly partonic stages of the reaction. Direct photons are distinguished from the bulk of photons as those coming from collisions and not decays.

Unfortunately, the overwhelming amount of photons in heavy-ion collisions comes from hadronic decays in the late stages, mostly $\pi^0 \rightarrow \gamma\gamma$. These decay-photons impose a serious challenge for the experimental extraction of direct photon data. Up to now, several experiments have gone through the challenge to obtain the spectra of direct photons: Helios, WA80 and CERES (all at CERN-SPS) could publish upper limits, while WA98 (CERN-SPS) [8] and PHENIX (BNL-RHIC) [9, 10] have published explicit data points for direct photons.

On the theoretical side, calculations for the elementary photon production processes are known since long, see e.g. Kapusta *et al.* [11] and Xiong *et al.* [12]. The major

problem here is the difficulty to describe the time evolution of the produced matter, which is, up to now, not possible from first principle Quantum Chromodynamics (QCD). One has to rely on well-developed dynamical models to describe the space-time evolution of the nuclear interactions in the hot and dense stage of the reaction. A well-established approach to explore the dynamics of heavy-ion reactions is relativistic transport theory [13–21]. In this kind of microscopic description, the hadronic and/or partonic stage of the collision is described under certain approximations. Most transport models, for instance, cannot describe collisions with more than two incoming particles, which restricts the applicability to low particle densities, where multi-particle interactions are less important. Some attempts to include multi-particle interactions do exist [18, 22–26], but this field of study is still rather new. The coupling of a partonic phase with a hadronic phase poses another challenge on transport models, because the microscopic details of that transition are not well known. Another complication in the transport approach is that all microscopic scatterings are explicitly treated in the model and therefore the cross-sections for all processes must be known or extrapolated. However, for many processes high quality experimental data are not available, and therefore a large fraction of the cross-sections have to be calculated or parametrized by additional models.

Relativistic, (non-)viscous fluid- or hydrodynamics is a different approach to explore the space-time evolution of a heavy-ion collision [27–42]. It constitutes a macroscopic description of the matter that is created, assuming that at every time and in every place the matter is in local thermal equilibrium. This assumption can only be true if the matter is sufficiently dense, so in the late stages of a heavy-ion collision fluid-dynamics loses applicability. In addition, the requirement of local thermal equilibrium restricts the starting time of the hydrodynamic model. An advantage is that in the dense stages, hydrodynamics can propagate any kind of matter, and also allows for transitions between two types of matter, e.g. QGP and hadron gas, if an appropriate Equation of State (EoS) is provided. Fluid-dynamics can therefore be used to study hadronic and partonic matter in one common framework.

*Electronic address: baeuchle@th.physik.uni-frankfurt.de

The restrictions of these kinds of models can be loosened as well. By introducing viscosity and heat conductivity, perfect thermal equilibrium does not have to be present at any point. However, even with second order corrections the matter has to be close to equilibrium [43–45].

Input to solve the hydrodynamic differential equations are the boundaries, i.e. the initial state (the distributions of all relevant densities and currents at the time the evolution starts), the Equation of State providing the pressure as function of the energy and baryon densities, that describes the behaviour of the matter that is considered, and the freeze-out hypersurface.

Finally, approaches to the theoretical description of direct photon spectra may include calculations in perturbative Quantum-Chromo-Dynamics (pQCD). Calculations based on pQCD describe the high- p_\perp photon data in proton-proton collisions very well and, if scaled by the number of binary nucleon-nucleon collisions, also those in heavy-ion reactions. The range of applicability of these calculations is, however, limited to high transverse momenta $p_\perp^\gamma \gg 1$ GeV.

The different approaches have different applicability limits. E.g., thermal rates can only be applied if the assumption of local thermal equilibrium is fulfilled. Photon emission rates can then be calculated by folding the particle distribution functions of the participating particle species with the respective cross-sections. This framework can be applied to either static models, simplified hydrodynamics-inspired models such as the blast wave model and to full fluid-dynamic calculations. The space-time evolution of a reaction as predicted by microscopic theories can be averaged over in order to apply thermal rates to the coarse-grained distributions [39]. The application of microscopic cross-sections can only be undertaken in a model where all microscopic collisions are known. That limits the field of use to transport models. For previous calculations of photon spectra from transport models see e.g. [46–48].

In this paper, we investigate the spectra of direct photons coming from microscopic hadronic scatterings, thermal hadronic and partonic emission and hard initial pQCD scatterings. We compare results from a purely microscopic model to those from an integrated micro+macro hydrodynamic approach that embeds a hydrodynamic phase into the UrQMD approach. The paper is organized as follows. First, we explain the hybrid model (Section II). In the following Section III, we elaborate on the photon sources considered in our model. In Sections IV, V and VI, we apply our model to compare thermal rates from microscopic theory to those from the literature, compare different physics assumptions with experimental data from the WA98 collaboration [8] and analyse the sources of photon emission.

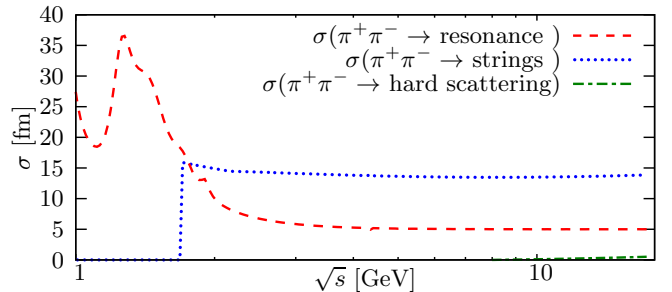


FIG. 1: (Color Online.) UrQMD-cross-sections for $\pi^+\pi^-$ -collisions as function of center-of-mass energy. We show the resonant hadronic cross-section (red dashed line), the cross-section for the formation of strings (blue dotted line) and for hard scatterings via PYTHIA (green dash-dotted line). The peak at the ρ -meson pole mass has been cut out for better visibility.

II. THE HYBRID MODEL

A. Transport model

UrQMD v2.3 (Ultra-relativistic Quantum Molecular Dynamics) is a microscopic transport model [14, 15, 49]. It includes all hadrons and resonances up to masses $m \approx 2.2$ GeV and at high energies can excite and fragment strings. The cross-sections are either parametrized, calculated via detailed balance or taken from the additive quark model (AQM), if no experimental values are available. At high parton momentum transfers, PYTHIA [50] is employed for pQCD scatterings.

UrQMD differentiates between two regimes for the excitation and fragmentation of strings. Below a momentum transfer of $Q < 1.5$ GeV a maximum of two longitudinal strings are excited according to the LUND picture, at momentum transfers above $Q > 1.5$ GeV hard interactions are modelled via PYTHIA. Figure 1 shows the total cross-sections of resonant hadronic interactions, string excitation and (hard) PYTHIA-scatterings as a function of the center-of-mass energy of the collision \sqrt{s}_{coll} . The contribution of hard scatterings to the total $\pi^+\pi^-$ cross-section at the highest SPS-energies ($\sqrt{s} \approx 17.3$ GeV) is about 4 %. Figure 2 shows a comparison between charged particle spectra from proton-proton collisions calculated in UrQMD with and without the PYTHIA contribution. For detailed information on the inclusion of PYTHIA, the reader is referred to Section II of [49].

In the UrQMD framework, all particle properties (mass, width, spectral shape) are taken at their vacuum values, the propagation is performed without potentials (cascade mode). UrQMD has been used by Dumitru *et al.* to study direct photon emission earlier [46]; a brief comparison between their results and the results obtained with this approach can be found in Appendix C.

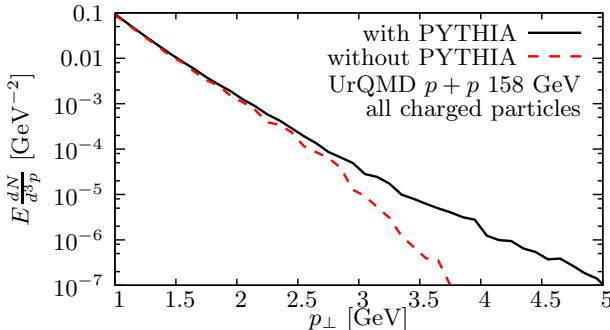


FIG. 2: (Color Online.) Charged particle spectra from proton-proton-collisions at $E_{\text{lab}} = 158$ GeV calculated with UrQMD with (solid black line) and without (dashed red line) PYTHIA.

B. Hybrid model

In the following, we compare results from this microscopic model to results obtained with a hybrid model description [51]. Here, the high-density part of the reaction is modelled using ideal 3+1-dimensional fluid-dynamics. The unequilibrated initial state and the low-density final state are described by UrQMD. Thus, those stages are mainly governed by string dynamics (initial state) and hadronic rescattering (final state).

To connect the initial transport phase to the fluid-dynamic phase, the baryon-number-, energy- and momentum-densities are smoothed and put into the hydrodynamic calculation after the incoming nuclei have passed through each other. Note that in non-central collisions, the spectators are propagated in the cascade. Thus, the initial state for the hydrodynamic stage is subject to both geometrical and event-by-event fluctuations. Temperature, chemical potential, pressure and other macroscopic quantities are determined from the densities by the Equation of State (EoS) used in the current calculation. During this transition, the system is forced into an equilibrated state, regardless of the actual level of equilibration before the transition. The initial temperature profile at $z = 0$ for a sample $Pb + Pb$ -event with $b = 0$ fm and $E_{\text{Lab}} = 158$ AGeV for two different EoS (Bag Model and Hadron Gas) is shown in Figure 3. Then the ideal (3+1) dimensional hydrodynamic equations are solved on a grid using the SHASTA-algorithm [36].

After the local rest frame energy density has dropped below a threshold value of $\epsilon_{\text{crit}} = 730$ MeV/fm³ ($\approx 5\epsilon_0$), particles are created on an isochronous hyper-surface from the densities by means of the Cooper-Frye formula and propagation is continued in UrQMD.

The transition scenario chosen for the present studies is always isochronous, i.e. the whole system must meet the criterion at the same calculational-frame time before the transition is performed. Earlier investigations within this hybrid model include an extensive analysis of the effect of changing the transition criterion [51], strangeness

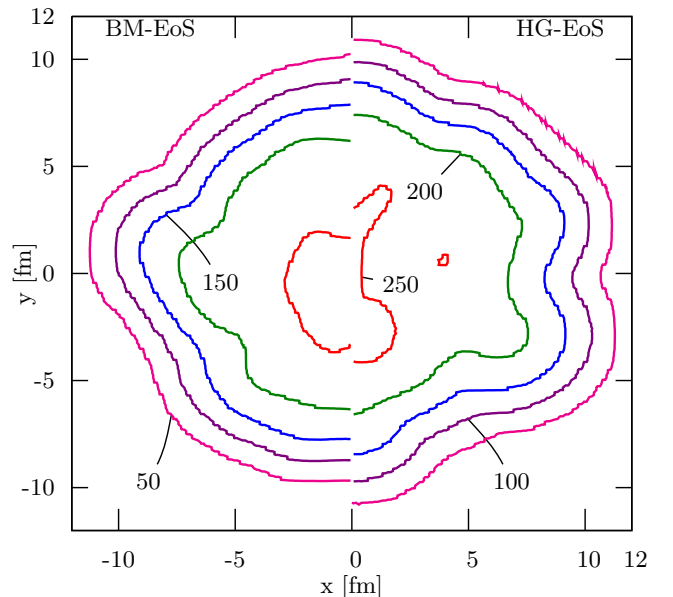


FIG. 3: (Color Online). Temperature profiles after switching to fluid-dynamic description, calculated with the Bag model (left half) and hadron gas Equation of State (right half). Along the lines, the temperature is constant, going from $T = 50$ MeV at the outermost line to $T = 250$ MeV at the innermost. Calculations have been done for $Pb + Pb$ -collisions at $E_{\text{Lab}} = 158$ AGeV with $b = 0$ fm.

production [52, 53], HBT correlations [54], transverse mass [55] and elliptic flow [56].

C. Equations of State

For the investigations presented here, different Equations of State are used for the hydrodynamic phase. The base line calculations are done with a hadron gas Equation of State (HG-EoS), which includes the same degrees of freedom as present in the transport phase. This allows to explore the effects due to the change of the dynamic description. Secondly, a MIT-Bag model EoS (BM-EoS) with a partonic phase and a first order phase transition [36] is employed. The BM-EoS thus allows for investigations of photon emission from the QGP. In order to obtain meaningful values of temperature and chemical potentials from the densities, the BM-EoS is smoothly transferred to the HG-EoS just above the transition energy density.

III. PHOTON EMISSION SOURCES

Photon emission is calculated perturbatively in both scenarios, hydrodynamics and transport, because the evolution of the underlying event is not altered by the emission of photons due to their very small emission probability. The channels considered for photon emission

may differ between the hybrid approach and the binary scattering model. Emission from a Quark-Gluon-Plasma can only happen in the hydrodynamic phase, and only if the Equation of State used has partonic degrees of freedom. Photons from baryonic interactions are neglected in the present calculation. Emission of hard photons from early pQCD-scatterings of nucleons is calculated separately and incoherently added to the simulated spectra.

A. Photons from microscopic collisions

In the transport part of the (hybrid) model, each scattering is examined and the cross-section for photon emission is calculated. Here, we employ the well-established cross-sections from Kapusta *et al.* [11] and Xiong *et al.* [12]. Kapusta and collaborators based their calculations on the photon self-energy derived from a Lagrange density involving the pion, ρ and photon-fields

$$\mathcal{L} = |D_\mu \Phi|^2 - m_\pi^2 |\Phi|^2 - \frac{1}{4} \rho_{\mu\nu} \rho^{\mu\nu} + \frac{1}{2} m_\rho^2 \rho_\mu \rho^\mu - \frac{1}{4} F_{\mu\nu} F^{\mu\nu} . \quad (1)$$

Here, Φ is the pion field, $\rho_{\mu\nu} = \partial_\mu \rho_\nu - \partial_\nu \rho_\mu$ and $F_{\mu\nu} = \partial_\mu A_\nu - \partial_\nu A_\mu$ are the ρ and photon field-strength tensors and $D_\mu = \partial_\mu - ieA_\mu - ig_\rho \rho_\mu$ is the covariant derivative. The ρ decay constant g_ρ is calculated from the total width Γ_{tot}^ρ of the ρ meson:

$$g_\rho^2 = 48\pi \frac{\Gamma_{\text{tot}}^\rho m_\rho^2}{\left(\sqrt{m_\rho^2 - 4m_\pi^2}\right)^3} . \quad (2)$$

The differential cross-sections used for the present investigation [11, 12] are given in Appendix D.

All scatterings during the transport phase are examined in order to obtain direct photon spectra. For every scattering that may produce photons (i.e. those that have initial states equal to the processes listed in Appendix D), the corresponding fraction of a photon,

$$N_\gamma = \frac{\sigma_{\text{em}}}{\sigma_{\text{tot}}} , \quad (3)$$

is produced. Here, σ_{tot} is the sum of the total hadronic cross-section for a collision with these ingoing particles (as provided by UrQMD) and the electromagnetic cross-section σ_{em} as calculated by the aforementioned formulæ. In order to obtain the correct angular distribution of the produced photons and to enhance statistics, for each scattering many fractional photons are created that populate all kinematically allowed momentum transfers t . In this procedure, each photon is given a weight ΔN_γ^t according to

$$\Delta N_\gamma^t = \frac{\frac{d\sigma_{\text{em}}}{dt}(s, t) \Delta t}{\sigma_{\text{tot}}(s)} , \quad (4)$$

and the photons are distributed evenly in the azimuthal angle φ . The integral $\sigma_{\text{em}}(s) = \int d\sigma_{\text{em}}/dt dt$ is performed analytically for each channel. The resulting formulæ are shown in Appendix E.

Since the width of the ρ -meson is not negligible, its mass distribution has to be taken into account. For the processes with a ρ -meson in the initial state, the actual mass $m_\rho = \sqrt{p_\mu p^\mu}$ of the incoming meson is used for the calculation of the cross-section. If there is a ρ -meson in the final state, then first the mass of the ρ is chosen randomly according to a Breit-Wigner distribution with mass-dependent width. This mass is then used for all further calculations of this process. Figure 4 shows the cross-sections of the channels listed above as a function of \sqrt{s} .

B. Photons from hydrodynamics

In the hydrodynamic phase photons are produced fractionally from every cell on the hydrodynamic grid whose energy density is above a threshold $\varepsilon_{\text{thr}} = 10^{-12} \varepsilon_0$ using the parametrizations by Turbide, Rapp and Gale [57]. They use an effective non-linear σ -model Lagrange density in which the vector and axial vector fields are implemented as massive gauge fields of the chiral $U(3)_L \times U(3)_R$ symmetry to obtain the rates. For details on this ansatz, the reader is referred to the original publication [57].

As mentioned earlier, the processes calculated by Turbide *et al.* differ from those considered by Kapusta *et al.* Only the processes $\pi\pi \rightarrow \gamma\rho$ and $\pi\rho \rightarrow \gamma\pi$ are therefore common in both models. The rate of Turbide *et al.* for $\pi\rho \rightarrow \gamma\pi$ directly includes the process with an intermediate a_1 -meson.

To simplify the calculations, all photon rates in [57] are parametrized by the general form

$$E \frac{dR}{d^3 p} = A \exp \left(\frac{B}{(2ET)^C} - D \frac{E}{T} \right) , \quad (5)$$

where A , B , C and D are linear functions of some power of the temperature T : $A(T) = A_1 + A_2 T^{A_3}$. The parameter set can be obtained from [57]. In the rates, the energy E and temperature T are to be given in units of GeV, and the result will have the unit $\text{GeV}^{-2} \text{fm}^{-4}$. We also employ the hadronic form factor introduced in [57].

In the Quark-Gluon-Plasma, the rate used is taken from Ref. [58]. They computed the full leading-order result as

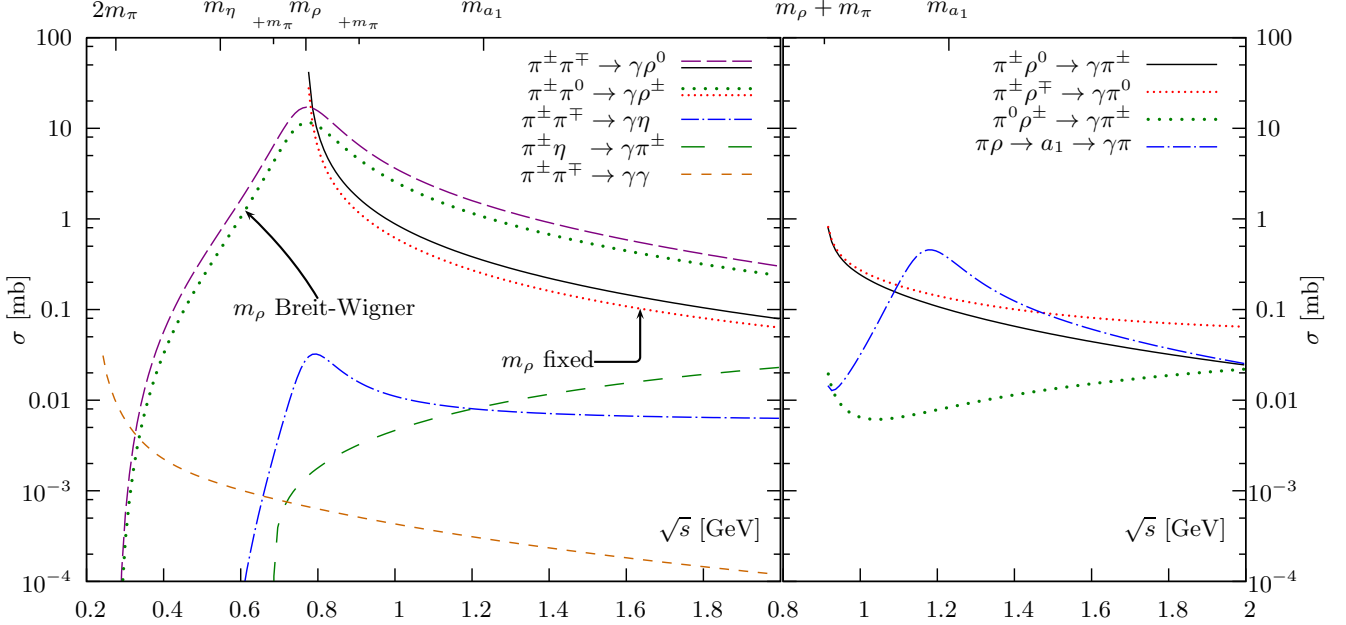


FIG. 4: (Color Online.) Cross-sections for all included channels as a function of \sqrt{s} . For visibility, the cross-sections for all processes $\pi\rho \rightarrow \gamma\pi$ are shown separately. They have been calculated with a ρ mass $m_\rho = 0.769$ GeV. The left plot shows the cross-sections for $\pi\pi \rightarrow \gamma\rho$ both for fixed ρ mass ($m_\rho = 0.769$ GeV, labelled “ m_ρ fixed”) and for variable ρ mass (labelled “ m_ρ Breit-Wigner”).

$$E \frac{dR}{d^3p} = \sum_{i=1}^{N_f} q_i^2 \frac{\alpha_{\text{em}} \alpha_S}{2\pi^2} T^2 \frac{1}{e^x + 1} \left(\ln \left(\frac{\sqrt{3}}{g} \right) + \frac{1}{2} \ln(2x) + C_{22}(x) + C_{\text{brems}}(x) + C_{\text{ann}}(x) \right), \quad (6)$$

and give convenient parametrizations for the contribution of $2 \leftrightarrow 2$ -, bremsstrahlung- and annihilation-processes (C_{22} , C_{brems} and C_{ann} , respectively)

$$C_{22}(x) = 0.041x^{-1} - 0.3615 + 1.01 \exp(-1.35x) \quad (7a)$$

$$C_{\text{brems}}(x) + C_{\text{ann}}(x) = \sqrt{1 + \frac{N_f}{6}} \left[\frac{0.548 \ln(12.28 + \frac{1}{x})}{x^{\frac{3}{2}}} + \frac{0.133x}{\sqrt{1 + \frac{x}{16.27}}} \right]. \quad (7b)$$

In Equations (6) and (7), $x = E/T$, q_i is the charge of quark-flavour i , α_{em} and $\alpha_S = g^2/4\pi$ are the electromagnetic and QCD coupling constants, respectively. In our calculations, we use $N_f = 3$, and therefore $\sum_i q_i^2 = 2/3$. The temperature dependence of α_S is taken from [59] as

$$\alpha_S(T) = \frac{6\pi}{(33 - 2N_f) \ln \left(\frac{8T}{T_C} \right)}, \quad (8)$$

and the critical temperature at $\mu_B = 0$ to be $T_C = 170$ MeV.

C. Photons from primordial pQCD-scatterings

At high transverse momenta, a major contribution to the photon yield is the emission of photons from hard pQCD-scatterings of the partons in the incoming protons. In the intermediate and low p_\perp -regions, the contribution may be comparable to or smaller than the yield from other sources.

We apply the results extracted by Turbide *et al.* [57]. They first scale the photon spectrum from proton-proton-collisions by the number of binary collisions in Pb+Pb-collisions, and then add a Gaussian-shaped additional k_\perp -smearing to the result. The width of the Gaussian is obtained by fitting this procedure to the data from proton-nucleus collisions. The results shown here are ob-

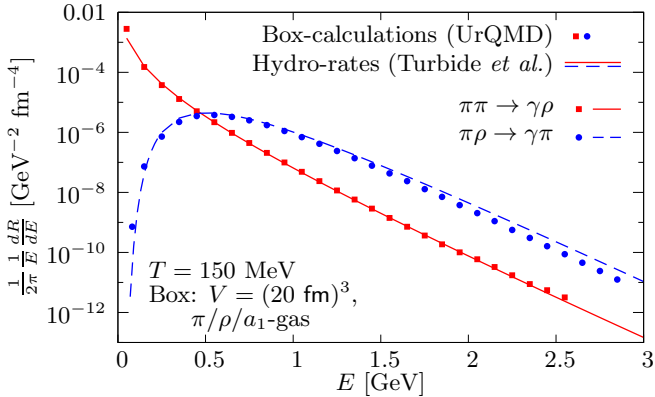


FIG. 5: (Color Online.) Comparisons between the rates from [57] (lines) and box calculations restricted to a π, ρ, a_1 -system (points) with UrQMD at $T = 150$ MeV.

tained with a $\langle \Delta k_\perp^2 \rangle = 0.2$ GeV 2 .

For comparison, we also show pQCD spectra obtained earlier by Gale [60] following Wong *et al.* [61]. They follow the same procedure as explained above. The authors of [60] obtain a higher intrinsic transverse parton momentum of $\langle \Delta k_\perp^2 \rangle = 0.9$ GeV 2 , yet lower spectra.

In order to compare our calculations to experimental data in Figure 14, we use the newer calculations by Turbide *et al.* [57].

IV. RATES FROM TRANSPORT AND HYDRODYNAMICS

Before comparing photon spectra from complex nucleus-nucleus collisions between cascade- and hybrid model, we check if both approaches give similar results for the setup of a fully thermalized box.

I.e., we perform UrQMD calculations in a box [62], allowing only π -, ρ - and a_1 -mesons to be present and to scatter. When the matter in the box has reached thermal and chemical equilibrium, the rate of photon emission is extracted based on the microscopic scatterings with the procedure described in Section III A. Then, we compare the microscopic rates to the hydrodynamic rates from Equation (5) with the parameters from [57]. Since the available rates in the cascade and hydrodynamic modes differ, as pointed out above, we restrict the comparison to the common rates $\pi\pi \rightarrow \gamma\rho$ and $\pi\rho \rightarrow \gamma\pi$. The cascade-rates are explicitly summed over all charge combinations.

Figure 5 shows the comparison of the rates at a temperature $T = 150$ MeV. It can be seen that the microscopically obtained rates agree very well with the thermodynamic rates.

V. PHOTON SPECTRA

A. Emission stages

For the present investigation, the evolution of a heavy-ion reaction is divided into three stages: “initial stage”, “intermediate stage” and “final stage”. The time spans of these stages are defined by the calculations in the hybrid model as before ($t < 1.4$ fm), during (1.4 fm $< t < 13.25$ fm for the hadron gas and cascade calculations and 1.4 fm $< t < 30$ fm for the Bag model calculations), and after the hydrodynamic description ($t > 13.25$ fm (HG, cascade) and $t > 30$ fm (BM)). I.e., the initial phase denotes the initial string dynamics until the transition to hydrodynamics. Since all differences between the models start at the transition to hydrodynamics, this stage and its contribution is always the same.

Secondly, the “intermediate stage” denotes the phase described by hydrodynamics. It starts with the transition to hydrodynamics and ends with the transition back to the cascade. Within this stage, the degrees of freedom may be partonic, hadronic and partonic (in case of a Bag model EoS calculation) or hadronic (in all cases). The “final stage” starts at the transition from hydrodynamics to the cascade. On average this happens at 13.25 fm for the hadron gas EoS and 30 fm for the Bag model EoS. For pure transport calculations, this phase is also set to start at 13.25 fm, so that a comparison between hadron gas EoS and cascade calculations is possible. The degrees of freedom in the “final stage” are hadrons and resonances. The calculations are done with UrQMD in cascade mode, and proceed until the last collision has happened.

B. Influence of EoS and dynamics

The contributions of each of these phases to the final spectra are shown in Figure 6 for the pure cascade calculation and in Figure 7 for the hybrid calculation with the hadron gas EoS. In both figures, the black solid lines show the complete direct photon spectra, the green dash-dotted lines show the initial stage-contribution, the red dashed lines show the photon spectrum from the final phase and the blue dotted lines show the contribution from the intermediate stage. In the hybrid model, the evolution during the intermediate stage is calculated within the hydrodynamic framework. We find that the contribution from this intermediate phase (1.4 fm $< t < 13.25$ fm) is similar in both models. However, at high transverse momenta $p_\perp > 3$ GeV, the cascade calculation yields more photons from this intermediate time span. This can be related to imperfect thermalization of the system at the transition from the initial non-equilibrium state, which is forced to thermalization at the transition to the hydrodynamic phase, but preserved when doing cascade-only calculations. However, Figure 6 suggests photon emission towards high transverse momenta from the intermediate stage is in any case

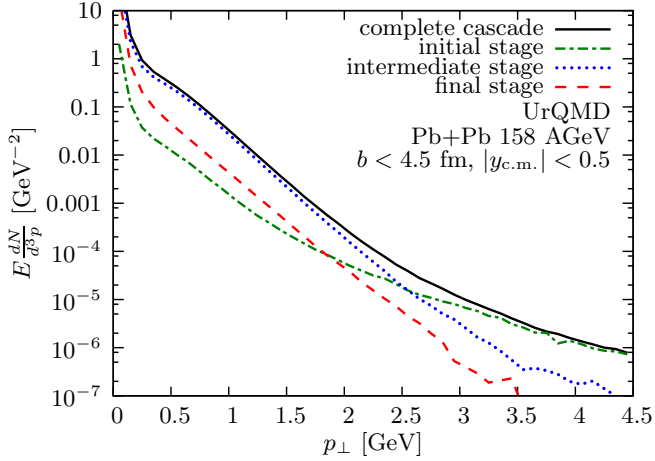


FIG. 6: (Color Online.) UrQMD calculation. Contributions of the initial ($t < 1.4$ fm, dash-dotted green line), intermediate (1.4 fm $< t < 13.25$ fm, dotted blue line) and final (13.25 fm $< t$, dashed red line) stages to the spectrum from pure cascade calculations (solid black line).

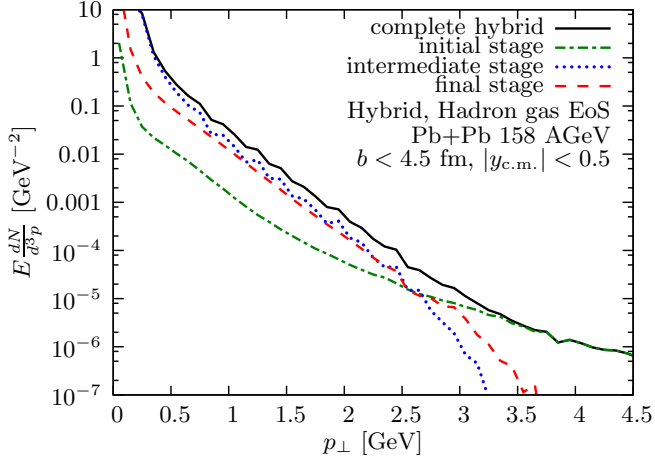


FIG. 7: (Color Online.) Hybrid model calculation with HG-EoS. Contributions of the initial (green dash-dotted line), intermediate (blue dotted line) and final (red dashed line) stages to the inclusive spectrum (solid black line). In the intermediate stage, the matter is described by hydrodynamics.

strongly suppressed with respect to photon emission from the initial stage. It is therefore justified to neglect non-equilibrium effects from the intermediate phase in the hybrid model. The major difference between cascade and hybrid model calculations is the magnitude of the contributions from the final stage (red dashed lines). Here, both models describe the system in the same way. The contribution from this phase to the hybrid model direct photon spectrum is very similar to the contribution from the intermediate stage. In the pure cascade calculation, on the contrary, the final phase contributes roughly a factor of 5 less to the spectrum than the intermediate stage does. A possible explanation for this is that the transi-

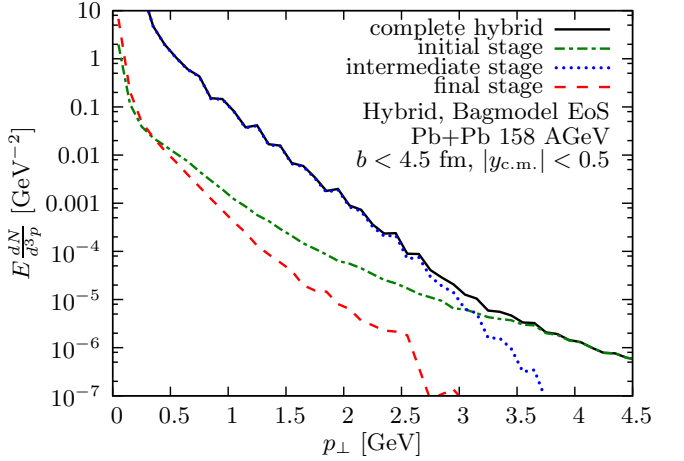


FIG. 8: (Color Online.) Hybrid model calculation with BM-EoS. Contributions to the initial (green dash-dotted line), intermediate (blue dotted line) and final (red dashed line) stages to the inclusive spectrum (solid black line). In the intermediate stage, the matter is described by hydrodynamics.

tion procedure from hydrodynamic to transport description enhances the number of meson-meson collisions in the late phase.

Interactions at early times ($t < 1.4$ fm) are a significant source of high transverse momentum $p_{\perp} > 3$ GeV photons. Here, the thermalized system of the later phase provides only minor contributions to the inclusive spectrum.

In the same analysis done for the hybrid model with the Bag model EoS (see Fig. 8), the picture is different. The contribution from the hydrodynamic intermediate stage is strongly enhanced, and the contribution of the final stage after the transition from the hydrodynamic phase is, in turn, reduced with respect to the cases presented before. The total photon spectrum is completely dominated by emission from the hydrodynamic phase at low and intermediate transverse photon momenta $p_{\perp} < 3$ GeV. This coincides with the observation that the length of the hydrodynamic phase in this model (≈ 29 fm) is much longer than in the calculations with hadron gas EoS (≈ 12 fm), due to the large latent heat in the setup with the Bag model EoS. At high transverse photon momenta, the initial stage non-equilibrium cascade phase dominates the spectrum, as in the other cases discussed above.

C. Channel decomposition

The contributions of the different channels to the hadronic calculations, both in the pure cascade mode and the hybrid approach with a hadron gas EoS, is shown in Figures 9 and 10. The dominant contributions in both models are very similar; at low transverse momenta $p_{\perp} < 0.5$ GeV, the process with two initial pi-

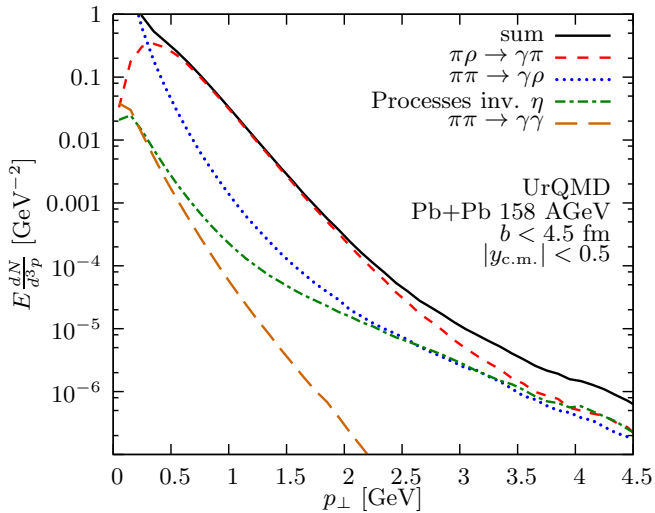


FIG. 9: (Color Online.) UrQMD calculation. Contributions of the different channels.

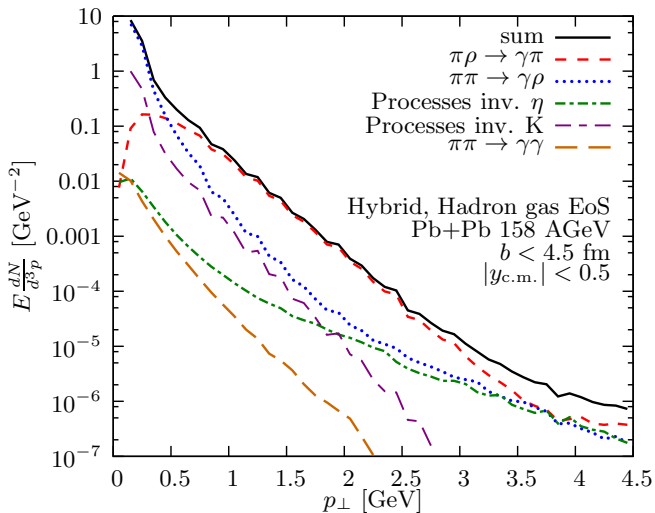


FIG. 10: (Color Online.) Hybrid model calculation with hadron gas EoS. Contributions of the different channels.

ons $\pi\pi \rightarrow \gamma\rho$ is dominant, while in the broad range of $0.5 \text{ GeV} < p_\perp < 3.5 \text{ GeV}$, $\pi\rho \rightarrow \gamma\pi$ is the major source of photons. Processes with an eta-meson ($\pi\pi \rightarrow \gamma\eta$ and $\pi\eta \rightarrow \gamma\pi$) become important at high transverse momenta, where they contribute in similar magnitude as the two aforementioned channels. Processes with kaons contribute less to the spectrum than the corresponding non-strange channels, and the process $\pi\pi \rightarrow \gamma\gamma$ is the least significant in all calculations, as expected.

In the photon spectrum extracted from the cascade calculation, one can observe a flattening of the spectrum at high transverse momenta $p_\perp \approx 3 \text{ GeV}$. At this point, $\pi\pi \rightarrow \gamma\rho$ and η -processes start to provide significant contributions to the photon spectrum and lead to a flatter slope already at $p_\perp \approx 2 \text{ GeV}$. In Section VI, we come back to this slope change and show it to be consistent

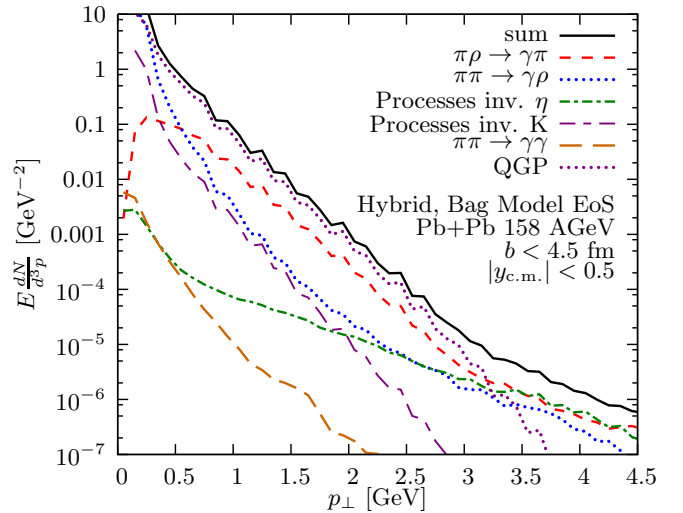


FIG. 11: (Color Online.) Hybrid model calculation with Bag model EoS. Contributions of the different channels in hybrid calculation with Bag model EoS.

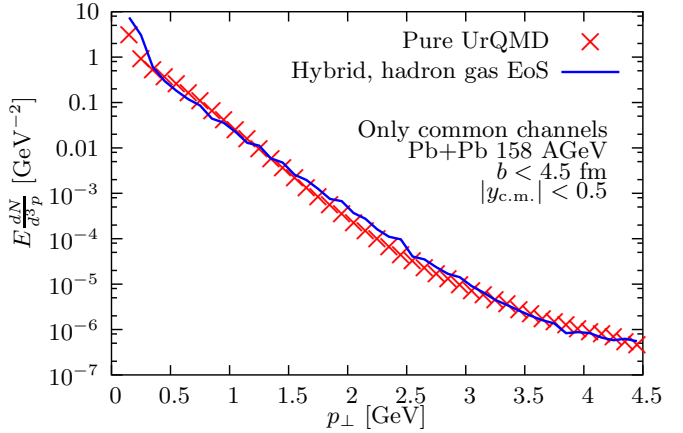


FIG. 12: (Color Online.) Comparison of direct photon spectra from the hybrid model with hadron gas EoS and transport model, using only common channels.

with the average emission times of the photons at these transverse momenta.

The calculations with the Bag model EoS yield a different picture (see Figure 11). Here, the dominant contribution comes from the Quark Gluon Plasma, whose emission magnitude is about two times higher than the combined contribution from all hadronic processes. Again, initial stage (pre-equilibrium) processes are dominant at high transverse momenta $p_\perp > 3 \text{ GeV}$. Apart from that, we observe a similar distribution among the reaction channels as we did above (see discussion of Figure 10); the process $\pi\rho \rightarrow \gamma\pi$ is dominant in the intermediate p_\perp -region, $\pi\pi \rightarrow \gamma\rho$ dominates the hadronic contribution at low p_\perp , the early scatterings in those channels and the channels involving η -mesons contribute to the high p_\perp -region in approximately equal amounts.

Figure 12 shows a comparison of hybrid model calcu-

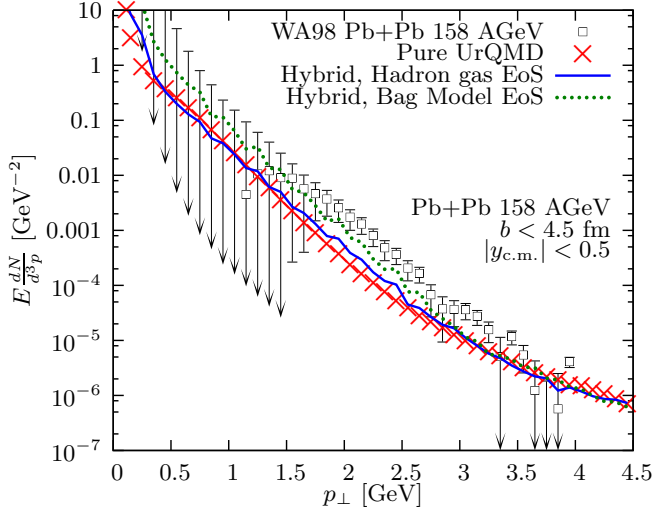


FIG. 13: (Color Online.) Comparison of the direct photon spectra from all variations of the model to the experimental data by the WA98-collaboration [8]. Calculations without intermediate hydrodynamic stage (pure cascade mode) are shown as red crosses, hybrid calculations with hadron gas EoS as red solid line and Bag model calculations are depicted by the dark-green dotted line. The data contain no photons from initial proton-proton collisions.

lations with hadron gas EoS and transport-calculations, using only common channels applied to a dynamic system (see Figure 5 for a static comparison). One observes that the direct photon spectrum is not sensitive to the change in the underlying dynamics (e.g. finite viscosities vs. ideal fluid) and indicates that even the two-body collision dynamic in UrQMD drives the system into equilibrium in the $\pi - \rho - a_1$ channel.

D. Comparison to data

A comprehensive comparison between the models presented above and experimental data is shown in Figure 13. Here, we show the sum over all channels and all stages in the cases of pure UrQMD-calculations and hybrid model with hadron gas and Bag model EoS. The Bag model Equation of State yields the highest photon spectra and provides a reasonable description of the data from the WA98-collaboration [8]. The purely hadronic calculations, with and without intermediate hydrodynamic calculation, give smaller yields than the scenario with a QGP.

After adding the pQCD-spectra as extracted by [57], we obtain Figure 14. Due to the rather large pQCD-contribution the difference between the spectra with varying EoS is reduced, and all calculations agree very well with the data.

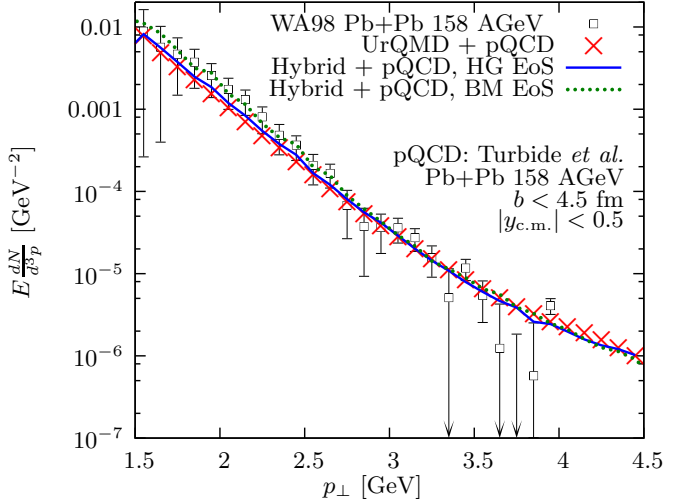


FIG. 14: (Color Online.) Comparison of the direct photon spectra from the model, with added pQCD-photons from [57], to the experimental data by the WA98-collaboration [8]. Calculations without intermediate hydrodynamic stage (pure cascade mode) are shown as red crosses, hybrid calculations with hadron gas EoS as red solid line and Bag model calculations are depicted by the dark-green dotted line.

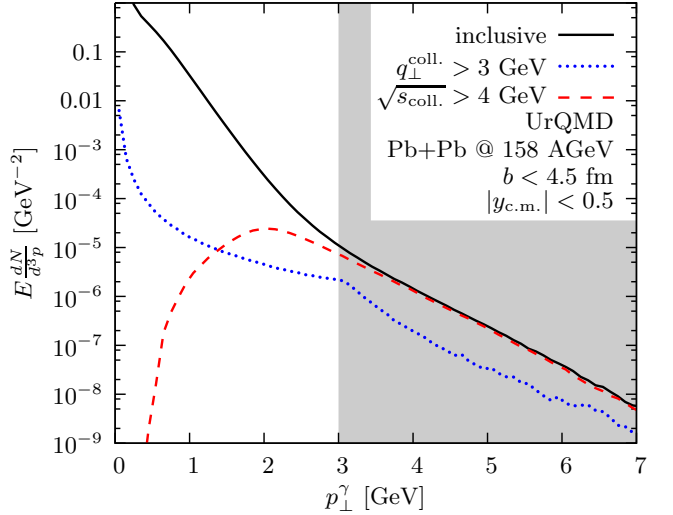


FIG. 15: (Color Online.) UrQMD calculation. The p_\perp -spectra for all photons (solid black line), photons from boosted collisions (dotted blue line) and collisions with high center-of-mass energy (dashed red line). The grey-shaded area indicates the range of the p_\perp -region used for the solid black lines in Figures 16 and 17.

VI. SENSITIVITY TO DIFFERENT EMISSION TIMES AND PROCESSES

To investigate the major sources for photons to the transverse momentum spectrum and to explore the sensitivity to the different reaction stages, we investigate the origin of the change of slope of the spectra at high transverse momenta $p_\perp \approx 3 \text{ GeV}$ in Figures 15, 16 and 17

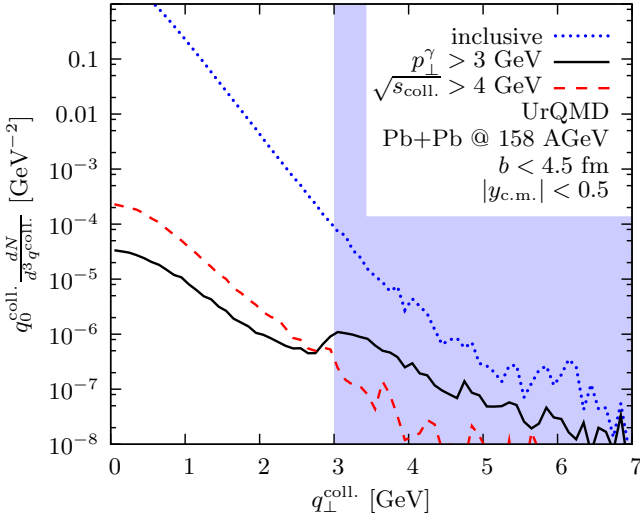


FIG. 16: (Color Online.) UrQMD calculation. The number of photons as a function of the transverse center-of-mass momentum of the elementary collision $q_{\perp}^{\text{coll.}}$. We show all photons (blue dotted line), photons that have high transverse momentum (black solid line) and photons from collisions with high center-of-mass energy (red dashed line). The light-blue-shaded area indicates the range of the q_{\perp} -region used for the dotted blue lines in Figures 15 and 17.

within UrQMD. Two processes may contribute to high p_{\perp} -photons: (I) collisions with a large \sqrt{s} in elementary reactions (i.e. early stage collisions) and (II) collisions of particles with large transverse flow q_{\perp} but rather small \sqrt{s} (i.e., late stage collisions). To disentangle these effects, we determine the contributions of scatterings with high center-of-mass energy $\sqrt{s} > 4 \text{ GeV}$ and high center-of-mass transverse momentum $q_{\perp} > 3 \text{ GeV}$. Figure 15 shows the transverse momentum spectrum of photons split up into the two contributions. Nearly all photons at high transverse momenta (grey-shaded area) come from collisions with high center-of-mass energies, whereas the contribution of high center-of-mass transverse momenta only shows a trivial structure at $p_{\perp} \approx q_{\perp}^{\text{threshold}} = 3 \text{ GeV}$.

One cross-check for Figure 15 is shown in Figure 16. Here, we observe that the collision spectrum is exponential. Only at high transverse boosts, a deviation from an exponential spectrum can be seen. This indicates that most photons with high transverse momentum come from unboosted collisions with $q_{\perp} < 1 \text{ GeV}$. The center-of-mass energy and transverse momentum of a collision show no correlation.

The latter can be seen in Figure 17, where the photon production rate is shown as a function of the center-of-mass energy of the individual collisions. The figure confirms the notion that most photons with high transverse momenta come from collisions with high center-of-mass energies. It is worthwhile to observe, however, that starting at $\sqrt{s}_{\text{coll.}} = 7 \text{ GeV}$, each elementary collision produces essentially only photons with transverse momenta $p_{\perp} > 3 \text{ GeV}$.

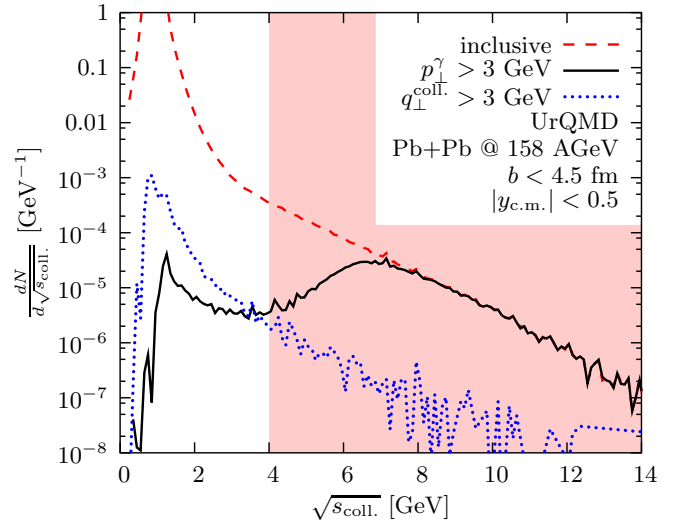


FIG. 17: (Color Online.) UrQMD calculation. The number of photons as a function of the center-of-mass energy of the elementary collision. We show all photons (red dashed line), photons that have high transverse momentum (black solid line) and photons from collisions of with high transverse center-of-mass momentum. The light-red-shaded area shows the range of the \sqrt{s} -region used for the red dashed lines in Figures 15 and 16.

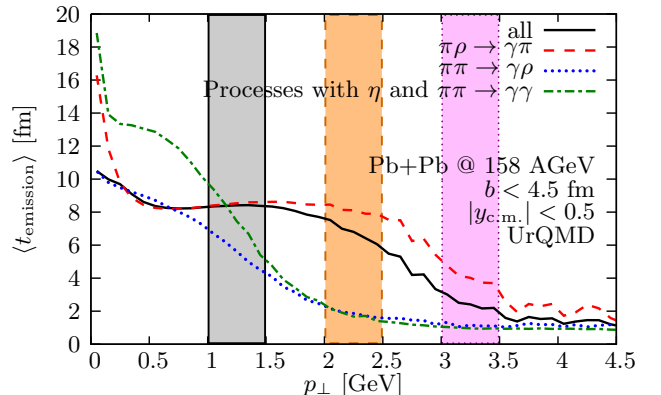


FIG. 18: (Color Online.) UrQMD calculation. Average photon emission times as a function of the transverse momentum for all photons, $\pi\rho \rightarrow \gamma\pi$ -, $\pi\pi \rightarrow \gamma\rho$ - and other processes (black solid, red dashed, blue dotted and green dash-dotted lines, respectively). The shaded areas correspond to the p_{\perp} -regions used for the curves shown in Figure 19.

The distribution of center-of-mass energies also shows that the vast majority of collisions happen around the ρ and a_1 -pole masses.

Figure 18 shows the average emission times of photons as a function of the transverse momentum for the various channels. It is noticeable that over a very broad momentum range, $0.3 \text{ GeV} < p_{\perp} < 2.1 \text{ GeV}$, the average emission time stays at a constant level of about $\langle t_{\text{emission}} \rangle \approx 8 \text{ fm}$. This coincides with the region where the process $\pi\rho \rightarrow \gamma\pi$ dominates. Only at high transverse

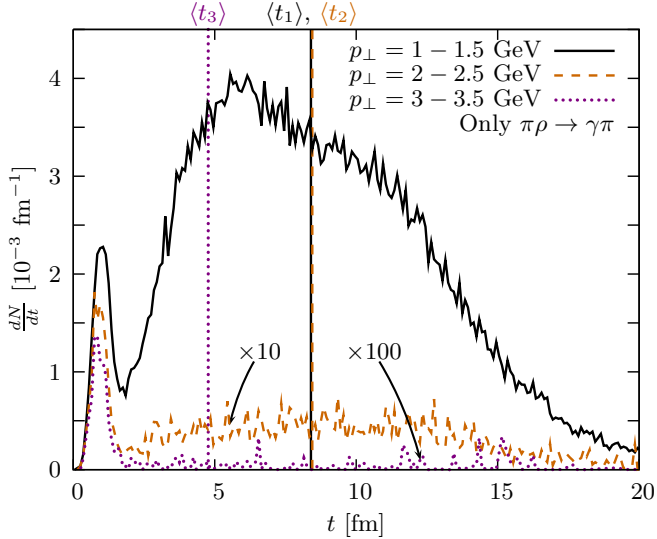


FIG. 19: (Color Online.) UrQMD calculation. Emission time distribution of photons from $\pi\rho$ -scatterings for the different photon transverse momentum regions indicated in Figure 18. The vertical lines indicate the average emission time in the corresponding p_{\perp} -bin.

momenta, the early times dominate. This is consistent with the findings in Section V, that the spectrum clearly shows two different temperatures, one in the region below $p_{\perp} = 2.5$ GeV and a different temperature above $p_{\perp} > 3$ GeV. It also explains why the spectral contributions from $\pi\pi \rightarrow \gamma\rho$ and η -processes show a much flatter slope already at $p_{\perp} \approx 2$ GeV. At late times, when the average center-of-mass energy has decreased, photons are predominantly produced at low transverse momenta.

In Figure 19, we show the emission time distribution of photons in various p_{\perp} -bins for the $\pi\rho \rightarrow \gamma\pi$ -processes. It is interesting to see that at all transverse momenta, there is an initial flash of photons emitted at very early times $t \approx 1$ fm. In the low p_{\perp} -bin $1 \text{ GeV} < p_{\perp} < 1.5 \text{ GeV}$, a very strong contribution from the bulk emission in the hot and dense stage between $t = 4$ fm and $t = 12$ fm raises the average emission time. In the intermediate p_{\perp} -region $2 \text{ GeV} < p_{\perp} < 2.5 \text{ GeV}$, the bulk contribution is greatly reduced and shines less bright than the initial flash. In the highest p_{\perp} -region $3 \text{ GeV} < p_{\perp} < 3.5 \text{ GeV}$, the late bulk contribution is small and the initial stage dominates. However, one should note that due to the long lifetime of the intermediate stage, the average emission times are shifted to higher values.

VII. SUMMARY

In this work, we have studied direct photon emission from hadronic and partonic sources within three different dynamical models. In Section III, we presented our model for photon emission from microscopic collisions (Subsection III A) and from thermal rates (Subsec-

tion III B). Then, we introduced the cross-sections and thermal rates used for the present calculations.

In Section IV, we showed that the emission rates from a thermalized microscopic cascade calculation agree very well with the thermal rates used in the hydrodynamic part of the present model. We discussed the contributions from the different stages before, during and after the high-density part of the evolution to the direct photon spectra for cascade calculations as well as hadron gas and Bag model hybrid calculations. It was found that the relative contributions of photons in the hybrid calculation with hadron gas EoS and cascade simulations are similar. In contrast, in the Bag model calculations the intermediate high-density hydrodynamic phase takes a much longer time and contributes substantially more to the photon spectra.

Investigations that differentiate between the different channels showed that the process $\pi\rho \rightarrow \gamma\pi$ is the dominant hadronic source for photon production at intermediate photon transverse momenta $0.5 \text{ GeV} < p_{\perp} < 3 \text{ GeV}$, while $\pi\pi \rightarrow \gamma\rho$ is dominant at low photon transverse momenta $p_{\perp} < 0.5 \text{ GeV}$, only.

When comparing the different variations of the model (see Fig. 13), we found that both the hybrid model and the cascade model can explain the spectra measured by the WA98-collaboration [8], if pQCD-photons are included. By comparison of Figures 12 and 13, we can also conclude that the photon yields from the hybrid-model calculation with hadron gas Equation of State and pure transport calculation are equal within uncertainties, if the same sets of channels is used in the calculations.

We also found that photons at high transverse momenta $p_{\perp} > 3$ GeV show a significantly flatter slope (and therefore higher effective temperature) than photons with lower p_{\perp} . This effect was attributed to higher center of mass-energies that produce these photons, and we find that it is not significantly influenced by elementary collisions that have a high center of mass-boost in transverse direction. The analysis of average photon emission times showed that photons at $p_{\perp} > 3$ GeV are emitted significantly earlier than at lower transverse momenta.

We also discussed different model assumptions (see Appendix A and B), namely photon emission from colliding string ends and compared those to pQCD-spectra. The result indicated that direct photon emission from string ends is restricted to the early phase of the collision where the medium is hot. Neglecting those collisions lowers the effective temperature at high transverse momenta $p_{\perp} > 2.5$ GeV. In any case, string end contributions can be neglected in comparison to the pQCD contribution.

We found that the inclusion of a finite width of the produced ρ -mesons is relevant only at low transverse momenta. I.e., only in the lowest p_{\perp} -bin, the effect of assigning the pole mass or a mass chosen randomly according to the spectral function is important.

VIII. OUTLOOK

The good agreement between the calculations presented here and the experimental data shows that the cascade+hydrodynamic hybrid model provides an excellent tool to explore the properties of QCD-matter at energies where the (onset of) deconfinement is expected. We plan to extend the investigation to a more realistic equation of state with chiral restoration, critical endpoint and rapid cross-over [63]. Also, the decays of short-lived mesons and baryons which cannot be subtracted by the experiment may play a major role in enhancing the direct photon spectra and will therefore be investigated.

Furthermore, direct photon emission will be investigated for the systems studied or planned to be studied at RHIC (PHENIX), LHC (ALICE), FAIR (CBM) and SIS-100 (HADES).

More differential observables like direct photon elliptic flow can also be explored in the present model.

IX. ACKNOWLEDGEMENTS

This work has been supported by the Frankfurt Center for Scientific Computing (CSC), the GSI and the BMBF. The authors thank Hannah Petersen for providing the hybrid- and Dirk Rischke for the hydrodynamic code, as well as Jan Steinheimer-Froschauer for the equation of state. B. Bäuchle gratefully acknowledges support from the Deutsche Telekom Stiftung and the Helmholtz Research School on Quark Matter Studies. This work was supported by the Hessian LOEWE initiative through the Helmholtz International Center for FAIR.

The authors thank Elvira Santini and Pasi Huovinen for valuable discussions and Klaus Reygers for experimental clarifications.

Appendix A: Discussion: String ends

In UrQMD, the leading particles from a string have a reduced cross-section during their formation time. For all other purposes, they are treated as hadrons. (Hadronic) scatterings of the string ends happen typically at high center-of-mass energies \sqrt{s} . Collisions from string ends can only produce photons if the collision of fully formed hadrons of the same type would produce photons. Thus, their contribution is treated as an addition to the prompt contribution from primordial nucleus-nucleus interactions. Photons from those collisions contribute significantly to the spectra at high transverse momenta. Since these particles are not fully formed hadrons, but effectively represent quarks or di-quarks, a hadronic treatment of those processes is questionable.

The effects of including the photons from colliding string ends, i.e. interaction of leading (di-)quarks, in the calculation can be seen in Figure 20. The spectrum obtained by neglecting the collision of string ends is expo-

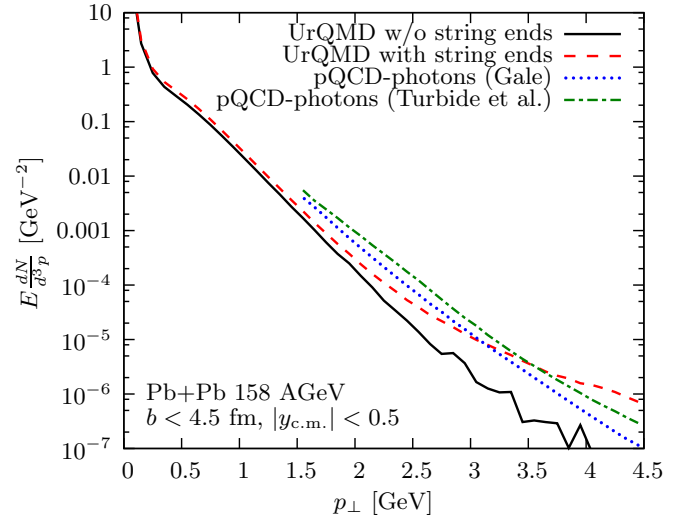


FIG. 20: (Color Online.) UrQMD calculation. Total yields of photons with (dashed line) and without (solid line) the contributions from colliding string ends. For comparison, the spectrum obtained from PYTHIA is shown as well.

nential and does not exhibit the flattening at high transverse photon momenta. The inclusion of (di-)quark scatterings, however, leads to a strong increase of the photon yield at high p_\perp . The contribution of pQCD-photons to the inclusive spectrum starts to be significant already at relatively low transverse photon momenta $p_\perp \approx 1$ GeV, although the magnitude of the contribution differs between the different parametrizations in [57] and [60].

Appendix B: Discussion: ρ -meson width

Earlier, we discussed the handling of the ρ -meson's finite width. Figure 21 shows the effects of following the calculation outlined there. In both channels, $\pi^\pm\pi^\mp \rightarrow \gamma\rho^0$ and $\pi^\pm\pi^0 \rightarrow \gamma\rho^\pm$, the yield is about 10 % higher for ρ s produced at their pole mass, and only at very low momenta this excess becomes as large as 40 %.

This behaviour can be explained by kinematic arguments: The by far highest scattering rate in $\pi + \pi$ -collisions is at $\sqrt{s} \approx m_\rho^0$. Here, the photon cross-section with fixed pole mass is much higher than the extended calculation with variable ρ mass. At all other center-of-mass energies, the extended model gives a higher cross-section, but these comparatively rare processes provide only a minor contribution to the spectrum. The processes at low \sqrt{s} will contribute primarily to the low- p_\perp -region, because the production of the ρ -meson consumes most of the available energy. Therefore, the enhancement in the model is most pronounced at low p_\perp .

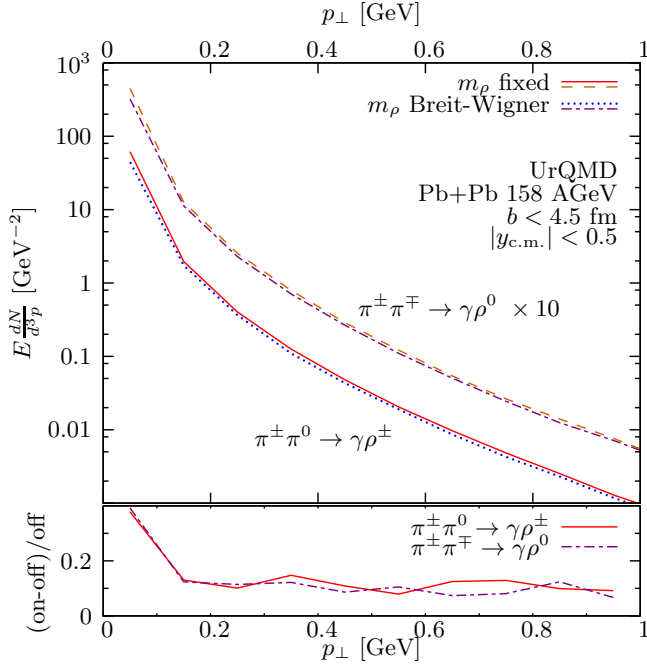


FIG. 21: (Color Online.) UrQMD calculation. Photon spectra from collisions that produce a ρ meson in the final state for the production of ρ mesons at its pole-mass (solid and dashed lines) and for the production of ρ mesons according to a Breit-Wigner-mass distribution (dotted and dash-dotted lines).

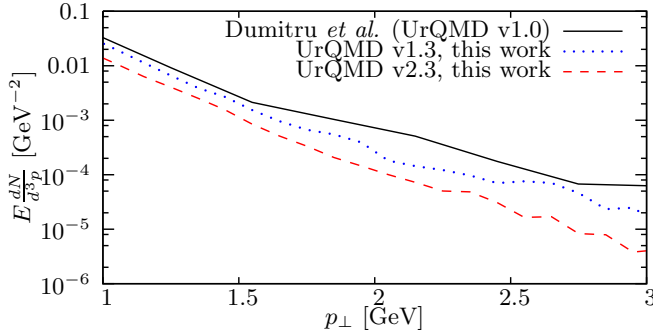


FIG. 22: (Color Online.) Comparison of the current model (red dashed line) to calculations from Dumitru *et al.* ([46], black solid line). For further comparison, we apply our model to an earlier UrQMD version (blue dotted line).

Appendix C: Comparison to older works with UrQMD

As mentioned in Section II, UrQMD has been used previously in order to obtain direct photon spectra [46]. The authors calculated transverse momentum spectra for central ($b = 0$ fm) Pb+Pb-collisions at $E_{\text{Lab}} = 160$ AGeV. Limiting ourselves to the same conditions, we can compare our work to that of Dumitru *et al.* In Figure 22, we compare results from the current UrQMD-version 2.3 to those obtained with the earlier versions 1.3 (using our own photon-analysis) and 1.0 (taken from [46]). The older UrQMD-versions yield significantly higher photon spectra at intermediate p_{\perp} .

We can identify two changes in UrQMD that lead to this behaviour. Between versions 1.0 (used by Dumitru *et al.*) and 1.3, the angular distributions of various processes have been altered. Since the collisions of pions with a high difference in rapidity provide significant contributions to the spectra from [46], the improved angular distributions reduce the photon production cross-section. Furthermore, in versions prior to 2.3, the number of pions has been unphysically high. The correction of this leads to fewer collisions involving pions and hence to a further reduction of the spectra.

Appendix D: Differential cross-sections

For completeness, we list the differential cross-sections for the processes used in [11, 12].

$$\frac{d\sigma}{dt} (\pi^{\pm} \pi^{\mp} \rightarrow \gamma \rho^0) = \frac{\alpha g_{\rho}^2}{4s p_{\text{c.m.}}^2} \left\{ 2 - (m_{\rho}^2 - 4m_{\pi}^2) \left[\frac{s - 2m_{\pi}^2}{s - m_{\rho}^2} \frac{1}{t - m_{\pi}^2} + \frac{m_{\pi}^2}{(t - m_{\pi}^2)^2} + (t \leftrightarrow u) \right] \right\} , \quad (\text{D1a})$$

$$\begin{aligned} \frac{d\sigma}{dt} (\pi^{\pm} \pi^0 \rightarrow \gamma \rho^{\pm}) = & -\frac{\alpha g_{\rho}^2}{16s p_{\text{c.m.}}^2} \left[\frac{(s - 2m_{\rho}^2)(t - m_{\pi}^2)^2}{m_{\rho}^2(s - m_{\rho}^2)^2} + \frac{(s - 6m_{\rho}^2)(t - m_{\pi}^2)}{m_{\rho}^2(s - m_{\rho}^2)} + \frac{4s(m_{\rho}^2 - 4m_{\pi}^2)}{(s - m_{\rho}^2)^2} \right. \\ & \left. + \frac{4(m_{\rho}^2 - 4m_{\pi}^2)}{t - m_{\pi}^2} \left(\frac{s}{s - m_{\rho}^2} + \frac{m_{\pi}^2}{t - m_{\pi}^2} \right) + \frac{m_{\pi}^2}{m_{\rho}^2} - \frac{9}{2} + (t \leftrightarrow u) \right] , \end{aligned} \quad (\text{D1b})$$

$$\frac{d\sigma}{dt} (\pi^\pm \rho^0 \rightarrow \gamma \pi^\pm) = \frac{\alpha g_\rho^2}{12 s p_{\text{c.m.}}^2} \left[2 - \frac{s(m_\rho^2 - 4m_\pi^2)}{(s - m_\pi^2)^2} - \frac{(m_\rho^2 - 4m_\pi^2)}{t - m_\pi^2} \left(\frac{s - m_\rho^2 + m_\pi^2}{(s - m_\pi^2)(t - m_\pi^2)} + \frac{m_\pi^2}{(t - m_\pi^2)} \right) \right] , \quad (\text{D1c})$$

$$\begin{aligned} \frac{d\sigma}{dt} (\pi^\pm \rho^\mp \rightarrow \gamma \pi^0) &= -\frac{\alpha g_\rho^2}{48 s p_{\text{c.m.}}^2} \left\{ 4(m_\rho^2 - 4m_\pi^2) \left[\frac{t}{(t - m_\pi^2)^2} + \frac{u}{(u - m_\rho^2)^2} - \frac{m_\rho^2}{s - m_\pi^2} \left(\frac{1}{t - m_\pi^2} + \frac{1}{u - m_\rho^2} \right) \right] \right. \\ &\quad \left. + \left(3 + \frac{s - m_\pi^2}{m_\rho^2} \right) \frac{s - m_\pi^2}{u - m_\rho^2} - \frac{1}{2} + \frac{s}{m_\rho^2} - \left(\frac{s - m_\pi^2}{u - m_\rho^2} \right)^2 \right\} , \end{aligned} \quad (\text{D1d})$$

$$\begin{aligned} \frac{d\sigma}{dt} (\pi^0 \rho^\pm \rightarrow \gamma \pi^\pm) &= \frac{\alpha g_\rho^2}{48 s p_{\text{c.m.}}^2} \left[\frac{9}{2} - \frac{s}{m_\rho^2} - \frac{4s(m_\rho^2 - 4m_\pi^2)}{(s - m_\pi^2)^2} + \frac{(s - m_\pi^2)^2 - 4m_\rho^2(m_\rho^2 - 4m_\pi^2)}{(u - m_\rho^2)^2} \right. \\ &\quad \left. + \frac{1}{u - m_\rho^2} \left(5(s - m_\pi^2) - \frac{(s - m_\pi^2)^2}{m_\rho^2} - \frac{4(m_\rho^2 - 4m_\pi^2)(s - m_\pi^2 + m_\rho^2)}{s - m_\pi^2} \right) \right] , \end{aligned} \quad (\text{D1e})$$

$$\frac{d\sigma}{dt} (\pi^\pm \pi^\mp \rightarrow \gamma \eta) = \frac{\pi \alpha A |F_\pi(s)|^2}{16 m_\eta^2 m_\rho^4 s p_{\text{c.m.}}^2} [s(u - m_\pi^2)(t - m_\pi^2) - m_\pi^2(s - m_\eta^2)^2] , \quad (\text{D1f})$$

$$\frac{d\sigma}{dt} (\pi^\pm \eta \rightarrow \gamma \pi^\pm) = \frac{\pi \alpha A |F_\pi(u)|^2}{16 m_\eta^2 m_\rho^4 s p_{\text{c.m.}}^2} [u(s - m_\pi^2)(t - m_\pi^2) - m_\pi^2(u - m_\eta^2)^2] , \quad (\text{D1g})$$

$$\frac{d\sigma}{dt} (\pi^\pm \pi^\mp \rightarrow \gamma \gamma) = \frac{2\pi \alpha^2}{s p_{\text{c.m.}}^2} \left[1 + 2m_\pi^2 \left(\frac{1}{t - m_\pi^2} + \frac{1}{u - m_\pi^2} \right) + 2m_\pi^4 \left(\frac{1}{t - m_\pi^2} + \frac{1}{u - m_\pi^2} \right)^2 \right] . \quad (\text{D1h})$$

In these equations, $t = (p_\pi - p_\gamma)^2$ is always the momentum transfer from the pion to the photon [64] (unlike the convention used in [11]) and $p_{\text{c.m.}} = (2\sqrt{s})^{-1} \sqrt{s^2 - 2s(m_1^2 + m_2^2) + (m_1^2 - m_2^2)^2}$ is the three-momentum of the incoming particles in the center-of-mass frame (m_1 and m_2 being their masses). The value of A is, consistent with [11], $A = g_{\eta\rho\rho}^2 g_\rho^2 / 4\pi \gamma_\rho^2 = 4.7$, and the pion electromagnetic form factor is

$$F_\pi(s) = \frac{m_\rho^4}{(s - m_\rho^2) + \Gamma_\rho^2 m_\rho^2} .$$

In their 1992 paper, Xiong *et al.* [12] calculate the cross-section for the formation of an intermediate a_1 -meson during $\pi\rho$ -scattering, averaged over all possible charge combinations:

This channel is not included in Kapusta *et al.* Xiong *et al.* obtain this from a Lagrange-density involving only

the pion-, photon-, ρ - and a_1 -fields

$$\mathcal{L} = G_\rho a_1^\mu (g_{\mu\nu} (p_\pi \cdot p_\rho) - p_{\pi\mu} p_{\rho\nu}) \rho^\nu \Phi + G_\rho \frac{e}{g_\rho} a_1^\mu (g_{\mu\nu} (p_\pi \cdot p_\gamma) - p_{\pi\mu} p_{\gamma\nu}) A^\nu \Phi , \quad (\text{D2})$$

where $G_\rho = 14.8 \text{ GeV}^{-1}$. The partial widths of the a_1 , $\Gamma_{a_1 \rightarrow \pi\rho}$ and $\Gamma_{a_1 \rightarrow \gamma\pi}$, are estimated to be

$$\Gamma_{a_1 \rightarrow \pi\rho} = \frac{G_\rho^2 p_{\text{c.m.}}}{24\pi m_{a_1}^2} \left\{ \frac{m_\rho^2}{4s} [s - (m_\rho^2 - m_\pi^2)] + \frac{1}{2}(s - m_\rho^2 - m_\pi^2) \right\} \quad \text{and} \quad (\text{D3a})$$

$$\Gamma_{a_1 \rightarrow \gamma\pi} = \frac{G_\rho^2 \alpha p_{\text{c.m.}}}{12 g_\rho^2 m_{a_1}^2} (s - m_\pi^2) . \quad (\text{D3b})$$

Appendix E: Integrated Cross-sections

The integration over the cross-sections listed in appendix D yield the following results:

$$\sigma(\pi^\pm\pi^\mp \rightarrow \gamma\rho^0) = \frac{\alpha g_\rho^2}{4sp_{\text{c.m.}}^2} \left\{ 2\Delta t - (m_\rho^2 - 4m_\pi^2) \left[\frac{s - 2m_\pi^2}{s - m_\rho^2} \ln \frac{(t_- - m_\pi^2)}{(t_+ - m_\pi^2)} \right. \right. \\ \left. \left. + \frac{m_\pi^2 \Delta t}{(m_\pi^2 - t_+)(m_\pi^2 - t_-)} + (t_\pm \leftrightarrow u_\mp) \right] \right\} , \quad (\text{E1a})$$

$$\sigma(\pi^\pm\pi^0 \rightarrow \gamma\rho^\pm) = -\frac{\alpha g_\rho^2}{16sp_{\text{c.m.}}^2} \left[\frac{s - 2m_\rho^2}{m_\rho^2(s - m_\rho^2)^2} \frac{1}{3} (t_-^3 - t_+^3) + \frac{s - 6m_\rho^2}{m_\rho^2(s - m_\rho^2)^2} \frac{1}{2} (t_-^2 - t_+^2) \right. \\ \left. + \left(\frac{4s(m_\rho^2 - 4m_\pi^2)}{(s - m_\rho^2)^2} + \frac{m_\pi^2}{m_\rho^2} - \frac{9}{2} \right) \Delta t + \frac{4s(m_\rho^2 - 4m_\pi^2)}{(s - m_\rho^2)^2} \ln \frac{t_- - m_\pi^2}{t_+ - m_\pi^2} \right. \\ \left. + \frac{4m_\pi^2(m_\rho^2 - 4m_\pi^2) \Delta t}{(m_\pi^2 - t_+)(m_\pi^2 - t_-)} + (t_\pm \leftrightarrow u_\mp) \right] , \quad (\text{E1b})$$

$$\sigma(\pi^\pm\rho^0 \rightarrow \gamma\pi^\pm) = \frac{\alpha g_\rho^2}{12sp_{\text{c.m.}}^2} \left[2\Delta t - \frac{s(m_\rho^2 - 4m_\pi^2)}{(s - m_\pi^2)^2} \Delta t - (m_\rho^2 - 4m_\pi^2) \left(\frac{s - m_\rho^2 + m_\pi^2}{s - m_\pi^2} \ln \frac{t_- - m_\pi^2}{t_+ - m_\pi^2} \right. \right. \\ \left. \left. + \frac{m_\pi^2 \Delta t}{(m_\pi^2 - t_+)(m_\pi^2 - t_-)} \right) \right] , \quad (\text{E1c})$$

$$\sigma(\pi^\pm\rho^\mp \rightarrow \gamma\pi^0) = -\frac{\alpha g_\rho^2}{48sp_{\text{c.m.}}^2} \left\{ 4(m_\rho^2 - 4m_\pi^2) \left[\frac{m_\pi^2 \Delta t}{(u_+ - m_\rho^2)(u_- - m_\rho^2)} + \frac{m_\pi^2 \Delta t}{(t_+ - m_\pi^2)(t_- - m_\pi^2)} \right. \right. \\ \left. \left. + \ln \frac{u_+ - m_\rho^2}{u_- - m_\rho^2} + \ln \frac{t_- - m_\pi^2}{t_+ - m_\pi^2} - \frac{m_\rho^2}{s - m_\pi^2} \left(\ln \frac{t_- - m_\pi^2}{t_+ - m_\pi^2} + \ln \frac{u_+ - m_\rho^2}{u_- - m_\rho^2} \right) \right] \right. \\ \left. + (s - m_\pi^2) \left(3 + \frac{s - m_\pi^2}{m_\rho^2} \right) \ln \frac{u_+ - m_\rho^2}{u_- - m_\rho^2} + \Delta t \left(\frac{s}{m_\rho^2} - \frac{1}{2} - \frac{(s - m_\pi^2)^2}{(u_+ - m_\rho^2)(u_- - m_\rho^2)} \right) \right\} , \quad (\text{E1d})$$

$$\sigma(\pi^0\rho^\pm \rightarrow \gamma\pi^\pm) = \frac{\alpha g_\rho^2}{48sp_{\text{c.m.}}^2} \left[\Delta t \left(\frac{9}{2} - \frac{s}{m_\rho^2} - \frac{4s(m_\rho^2 - 4m_\pi^2)}{(s - m_\pi^2)^2} + \frac{(s - m_\pi^2)^2 - 4m_\rho^2(m_\rho^2 - 4m_\pi^2)}{(u_+ - m_\rho^2)(u_- - m_\rho^2)} \right) \right. \\ \left. + \left(5(s - m_\pi^2) - \frac{(s - m_\pi^2)^2}{m_\rho^2} - \frac{4(m_\rho^2 - 4m_\pi^2)(s - m_\pi^2 + m_\rho^2)}{s - m_\pi^2} \right) \ln \frac{u_+ - m_\rho^2}{u_- - m_\rho^2} \right] , \quad (\text{E1e})$$

$$\sigma(\pi^\pm\pi^\mp \rightarrow \gamma\eta) = \frac{\pi\alpha A |F_\pi(s)|^2}{16m_\eta^2 m_\rho^4 sp_{\text{c.m.}}^2} \left[(2m_\pi^2 + m_\eta^2 - s) \frac{s}{2} (t_+^2 - t_-^2) - \frac{s}{3} (t_+^3 - t_-^3) - m_\pi^2 (m_\eta^4 + s(m_\pi^2 - m_\eta^2)) \right] \quad (\text{E1f})$$

$$\sigma(\pi^\pm\eta \rightarrow \gamma\pi^\pm) = \frac{\pi\alpha A}{16m_\eta^2 sp_{\text{c.m.}}^2} \left\{ -m_\pi^2 [(t_- + u_-)(s - m_\pi^2) + (2m_\pi^2 - s)^2] I_0 \right. \\ \left. + [(s - m_\pi^2)(m_\pi^2 + t_- + u_-) - 2m_\pi^2(s - 2m_\pi^2)] \left[(t_- + u_- - m_\rho^2) I_0 + \frac{1}{2} I_1 \right] \right. \\ \left. - s [\Delta t + (t_- + u_- - m_\rho^2) I_1 + (t_- + u_- - m_\rho^2)^2 I_0 - m_\rho^2 \Gamma_\rho^2 I_0] \right\} , \quad (\text{E1g})$$

$$\sigma(\pi^\pm\pi^\mp \rightarrow \gamma\gamma) = \frac{2\pi\alpha^2}{sp_{\text{c.m.}}^2} \left\{ \Delta t + 2m_\pi^2 \left[\left(1 - \frac{2m_\pi^2}{s} \right) \ln \frac{t_- - m_\pi^2}{t_+ - m_\pi^2} + \frac{m_\pi^2 \Delta t}{(t_- - m_\pi^2)(t_+ - m_\pi^2)} + (t_\pm \leftrightarrow u_\mp) \right] \right\} \quad (\text{E1h})$$

$$\sigma(\pi\rho \rightarrow a_1 \rightarrow \gamma\pi) = 4p_1\omega \frac{d\sigma}{dt} (\pi\rho \rightarrow a_1 \rightarrow \gamma\pi) . \quad (\text{E1i})$$

In those equations, $t_\pm = m_1^2 - 2\omega(E_1 \pm p_1)$ are the minimal and maximal allowed momentum transfers, and

correspondingly $u_\pm = m_1^2 + m_2^2 + m_4^2 - s - t_\pm$, and Δt is a

shorthand for $t_- - t_+$. The indices 1, 2 and 4 denote the particles in the order given on the left hand side of the equations (3 is the photon). E_1 , p_1 and $\omega = E_3$ denote momentum and energy of the respective particles in the

center-of-mass frame. In the cross-section $\pi^\pm\eta \rightarrow \gamma\pi^\pm$ (Eq. (E1g)), the following notations have been used for simplicity:

$$I_0 = \frac{1}{m_\rho \Gamma_\rho} \left[\text{atan} \left(\frac{u_+ - m_\rho^2}{m_\rho \Gamma_\rho} \right) - \text{atan} \left(\frac{u_- - m_\rho^2}{m_\rho \Gamma_\rho} \right) \right] \quad \text{and} \quad (\text{E2a})$$

$$I_1 = \ln \left(\frac{(u_- - m_\rho^2)^2 + m_\rho^2 \Gamma_\rho^2}{(u_+ - m_\rho^2)^2 + m_\rho^2 \Gamma_\rho^2} \right) \quad . \quad (\text{E2b})$$

[1] J. W. Harris and B. Muller, Ann. Rev. Nucl. Part. Sci. **46** (1996) 71

[2] S. A. Bass, M. Gyulassy, H. Stoecker and W. Greiner, J. Phys. G **25** (1999) R1

[3] J. Adams *et al.* [STAR Collaboration], Nucl. Phys. A **757** (2005) 102

[4] B. B. Back *et al.*, Nucl. Phys. A **757** (2005) 28

[5] I. Arsene *et al.* [BRAHMS Collaboration], Nucl. Phys. A **757** (2005) 1

[6] K. Adcox *et al.* [PHENIX Collaboration], Nucl. Phys. A **757** (2005) 184

[7] C. Alt *et al.* [NA49 Collaboration], Phys. Rev. C **77** (2008) 024903

[8] M. M. Aggarwal *et al.* [WA98 Collaboration],

[9] S. S. Adler *et al.* [PHENIX Collaboration], Phys. Rev. Lett. **94** (2005) 232301

[10] A. Adare *et al.* [PHENIX Collaboration],

[11] J. I. Kapusta, P. Lichard and D. Seibert, Phys. Rev. D **44** (1991) 2774 [Erratum-ibid. D **47** (1993) 4171].

[12] L. Xiong, E. V. Shuryak and G. E. Brown, Phys. Rev. D **46** (1992) 3798

[13] K. Geiger, Comput. Phys. Commun. **104** (1997) 70

[14] S. A. Bass *et al.*, Prog. Part. Nucl. Phys. **41** (1998) 255 [Prog. Part. Nucl. Phys. **41** (1998) 225]

[15] M. Bleicher *et al.*, J. Phys. G **25** (1999) 1859

[16] W. Ehehalt and W. Cassing,

[17] D. Molnar and P. Huovinen, Phys. Rev. Lett. **94** (2005) 012302

[18] Z. Xu and C. Greiner, Phys. Rev. C **71** (2005) 064901

[19] Z. W. Lin, C. M. Ko, B. A. Li, B. Zhang and S. Pal, Phys. Rev. C **72** (2005) 064901

[20] G. Burau, J. Bleibel, C. Fuchs, A. Faessler, L. V. Bravina and E. E. Zabrodin, Phys. Rev. C **71** (2005) 054905

[21] S. A. Bass, T. Renk and D. K. Srivastava, Nucl. Phys. A **783** (2007) 367.

[22] H. W. Barz and B. Kampfer, Nucl. Phys. A **683** (2001) 594

[23] W. Cassing, Nucl. Phys. A **700** (2002) 618

[24] A. B. Larionov, O. Buss, K. Gallmeister and U. Mosel, Phys. Rev. C **76** (2007) 044909

[25] J. Bleibel, G. Burau, A. Faessler and C. Fuchs, Phys. Rev. C **76** (2007) 024912

[26] J. Bleibel, G. Burau and C. Fuchs, Phys. Lett. B **659** (2008) 520

[27] J. Cleymans and K. Redlich,

[28] L. D. McLerran, M. Kataja, P. V. Ruuskanen and H. von Gersdorff, Phys. Rev. D **34** (1986) 2755.

[29] H. Von Gersdorff, L. D. McLerran, M. Kataja and P. V. Ruuskanen, Phys. Rev. D **34** (1986) 794.

[30] M. Kataja, Z. Phys. C **38** (1988) 419.

[31] D. K. Srivastava and B. Sinha, Phys. Lett. B **261** (1991) 1.

[32] D. K. Srivastava, B. Sinha and T. C. Awes, Phys. Lett. B **387** (1996) 21.

[33] D. K. Srivastava, B. Sinha, M. Gyulassy and X. N. Wang, Phys. Lett. B **276** (1992) 285.

[34] D. K. Srivastava, J. Alam, S. Chakrabarty, S. Raha and B. Sinha, Phys. Lett. B **278** (1992) 225.

[35] J. Cleymans and H. Satz, Z. Phys. C **57** (1993) 135

[36] D. H. Rischke, Y. Pursun and J. A. Maruhn, Nucl. Phys. A **595** (1995) 383 [Erratum-ibid. A **596** (1996) 717]

[37] T. Hirano, Phys. Rev. C **65** (2002) 011901

[38] P. Huovinen, P. V. Ruuskanen and S. S. Rasanen, Phys. Lett. B **535** (2002) 109

[39] P. Huovinen, M. Belkacem, P. J. Ellis and J. I. Kapusta, Phys. Rev. C **66** (2002) 014903

[40] P. F. Kolb and U. W. Heinz, arXiv:nucl-th/0305084.

[41] C. Nonaka and S. A. Bass, Phys. Rev. C **75** (2007) 014902

[42] E. Frodermann, R. Chatterjee and U. Heinz, J. Phys. G **34** (2007) 2249

[43] K. Dusling and D. Teaney, Phys. Rev. C **77** (2008) 034905

[44] R. Baier, P. Romatschke and U. A. Wiedemann, Phys. Rev. C **73** (2006) 064903

[45] H. Song and U. W. Heinz, Phys. Rev. C **78** (2008) 024902

[46] A. Dumitru, M. Bleicher, S. A. Bass, C. Spieles, L. Neise, H. Stoecker and W. Greiner, Phys. Rev. C **57** (1998) 3271

[47] D. K. Srivastava and K. Geiger, Phys. Rev. C **58** (1998) 1734

[48] E. L. Bratkovskaya, S. M. Kiselev and G. B. Sharkov, Phys. Rev. C **78** (2008) 034905

[49] H. Petersen, M. Bleicher, S. A. Bass and H. Stocker, arXiv:0805.0567 [hep-ph].

[50] T. Sjostrand, S. Mrenna and P. Z. Skands, JHEP **0605** (2006) 026

[51] H. Petersen, J. Steinheimer, G. Burau, M. Bleicher and

H. Stocker, Phys. Rev. C **78** (2008) 044901

[52] J. Steinheimer, M. Mitrovski, T. Schuster, H. Petersen, M. Bleicher and H. Stoecker, Phys. Lett. B **676** (2009) 126

[53] H. Petersen, M. Mitrovski, T. Schuster and M. Bleicher, Phys. Rev. C **80** (2009) 054910

[54] Q. f. Li, J. Steinheimer, H. Petersen, M. Bleicher and H. Stocker, Phys. Lett. B **674** (2009) 111

[55] H. Petersen, J. Steinheimer, M. Bleicher and H. Stocker, J. Phys. G **36** (2009) 055104

[56] H. Petersen, J. Steinheimer, G. Bureau and M. Bleicher, Eur. Phys. J. C **62** (2009) 31.

[57] S. Turbide, R. Rapp and C. Gale, Phys. Rev. C **69** (2004) 014903

[58] P. B. Arnold, G. D. Moore and L. G. Yaffe, JHEP **0112** (2001) 009

[59] F. M. Liu and K. Werner, J. Phys. G **36** (2009) 035101

[60] C. Gale, Nucl. Phys. A **698** (2002) 143

[61] C. Y. Wong and H. Wang, Phys. Rev. C **58** (1998) 376

[62] M. Belkacem *et al.*, Phys. Rev. C **58** (1998) 1727

[63] J. Steinheimer, V. Dexheimer, H. Petersen, M. Bleicher, S. Schramm and H. Stoecker, arXiv:0905.3099 [hep-ph].

[64] All cases with two pions in the initial state are symmetric in $t \leftrightarrow u$. Therefore, it is not necessary to specify which pion is the reference for t .